



Nitrogen- and carbonyl-rich conjugated small-molecule organic cathode for high-performance sodium-ion batteries

Journal:	<i>Journal of Materials Chemistry A</i>
Manuscript ID	TA-ART-05-2022-003953.R1
Article Type:	Paper
Date Submitted by the Author:	26-Jun-2022
Complete List of Authors:	<p>Kuan, Hsuan-Cheng; National Cheng Kung University, Chemical Engineering; National Cheng Kung University, Hierarchical Green-Energy Materials Research Center</p> <p>Luu, Nhu; National Cheng Kung University, Chemical Engineering; National Cheng Kung University, Hierarchical Green-Energy Materials Research Center</p> <p>Ivanov, Alexander; Oak Ridge National Laboratory, Chemical Sciences Division</p> <p>Chen, Teng-Hao; National Cheng Kung University, Pharmacy</p> <p>Popovs, Ilja; Oak Ridge National Laboratory,</p> <p>Lee, Jui-Chin ; National Cheng Kung University, Core Facility Center</p> <p>Kaveevivitchai, Watchareeya; National Cheng Kung University, Chemical Engineering; National Cheng Kung University, Hierarchical Green-Energy Materials Research Center</p>

ARTICLE

Nitrogen- and carbonyl-rich conjugated small-molecule organic cathode for high-performance sodium-ion batteries

Hsuan-Cheng Kuan,^{‡a} Nhu T. H. Luu,^{‡a} Alexander S. Ivanov,^b Teng-Hao Chen,^c Ilja Popovs,^b Jui-Chin Lee^d and Watchareeya Kaveevivitchai^{*a}

Received 00th January 20xx,
Accepted 00th January 20xx

DOI: 10.1039/x0xx00000x

Organic-based cathode materials have attracted considerable attention for sustainable Na-ion batteries due to their great promise to overcome the issues arising from the insertion of large Na⁺ into the rigid structures of conventional transition-metal-containing inorganic electrodes. The structural flexibility as a result of weak intermolecular interactions and simple electron- and ion-storage mechanisms found in organic compounds ensure facile and reversible transport of Na ions. To address the general drawbacks of small-molecule organic electrodes such as material dissolution in commonly used organic electrolytes and poor electronic conductivity, we report the use of a nitrogen- and carbonyl-rich highly extended π -conjugated small molecule, hexaazatrianthrylene (HATA) embedded quinone (HATAQ), as cathode for sodium-ion batteries. The unique hydrogen bonds between highly functionalized conjugated HATAQ molecules allow supramolecular graphite-like 2D layered arrangements in the solid state which help facilitate the structural stability during long-term cycling and promote charge transfer. The compound delivers a capacity as high as 460 mAh g⁻¹ at 500 mA g⁻¹ and excellent capacity retention of 99 % (~138 mAh g⁻¹) after 5000 cycles at an extremely high rate of 60 A g⁻¹. The reaction kinetics and redox mechanism of the material have been elucidated by several characterization techniques together with density functional theory (DFT) studies. The insights gained in this work could pave the way for ultra-high-performance small-molecule organic cathodes for sustainable energy storage.

Introduction

The rapidly increasing need for large-scale energy storage especially for renewable energy smart grids has driven the search for better energy storage technologies.^{1,2} Lithium-ion batteries (LIBs) currently suffer several limitations such as lithium natural reserves/supplies, limited energy density which is becoming more challenging to increase, and high toxicity of non-renewable transition metals used in electrodes which has a serious impact on the environment during production and disposal.²⁻⁴ Consequently, the trend of post-LIBs is now focused more on sustainable electrodes materials.^{5,6} Sodium-based batteries have captured considerable attention due to inexhaustible resources and lower price of sodium and their environmental benignity.⁵

Similar to LIBs, the development of cathode materials for sodium-ion batteries (SIBs) has been dominated by inorganic transition-metal-containing compounds (e.g., layered metal

oxides and polyanions) which either show poor cycling stability and limited capacity or have slow Na-ion transport kinetics.^{5,7} These behaviors directly result from the insertion/extraction of relatively larger Na⁺ (1.02 Å vs. 0.76 Å for Li⁺), which induces volume change, lattice distortion and phase transition of rigid inorganic crystal structures in addition to sluggish diffusion of large-sized Na ions.^{1,7,8} Organic materials generally assembled by weak intermolecular interactions (e.g., hydrogen bonds and van der Waals forces) offer more flexible structures which could more easily facilitate the transport of large ions and provide high Na-ion mobility without significant volume change.⁸⁻¹⁰ Organic-based redox-active materials have simple electron- and ion-storage mechanisms via reversible coordination reaction which, as a result, are much less specific to the nature of the guest metal ions.^{7,11}

Organic compounds also have other desirable features such as abundant resources, sustainability, low toxicity, environmental friendliness, redox tunability, structural diversity, ease of synthesis and processing as well as recyclability.^{12,13} Redox-active organic small molecules have been widely investigated as electrode materials due to their lightweight which can lead to high theoretical capacity.¹⁴ However, material dissolution in electrolytes has prevented these organic molecules from wider adoption.¹⁵ Among several strategies used to improve their stability, polymerization is frequently utilized.¹⁶ Nevertheless, a large portion of redox-inactive moieties is usually introduced to link polymer chains, leading to a decrease in specific capacity.¹⁷

^a Department of Chemical Engineering, National Cheng Kung University, Tainan City 70101, Taiwan; Hierarchical Green-Energy Materials (HI-GEM) Research Centre, National Cheng Kung University, Tainan City 70101, Taiwan.

^b Chemical Sciences Division, Oak Ridge National Laboratory, Oak Ridge, P.O. Box 2008, TN 37831, USA.

^c School of Pharmacy, National Cheng Kung University, Tainan City 70101, Taiwan.

^d Core Facility Centre, National Cheng Kung University, Tainan City 70101, Taiwan.

[†] Electronic supplementary information (ESI) available: Detailed experimental procedures as well as additional computational and mechanistic data. For ESI or other electronic format, see DOI: 10.1039/x0xx00000x

[‡] These authors contributed equally to this work.

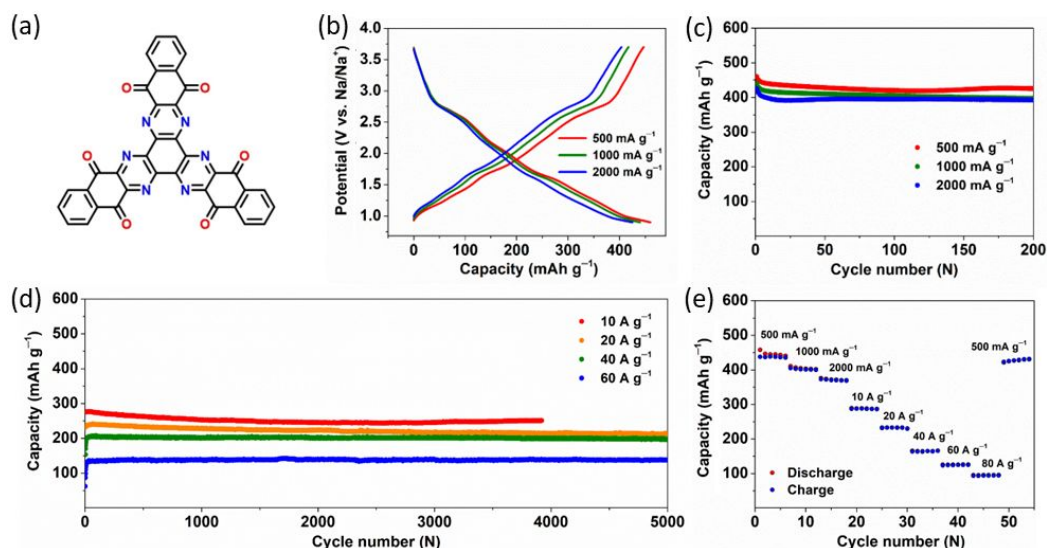


Fig. 1 (a) Chemical structure of small-molecule HATAQ cathode showing highly functionalized conjugated system of imine and carbonyl groups. (b) Discharge/charge profiles of HATAQ electrodes at current densities of 500 to 2000 mA g⁻¹ between 0.9 and 3.7 V. (c) and (d) Capacity retention at different rates up to 60 A g⁻¹. (e) Rate capability at various current densities.

In addition to these drawbacks of organic electrodes, poor electronic conductivity is another major issue slowing down their practical applications.¹⁵ Extended π -conjugated structures can help promote electronic conductivity and ensure sufficient charge transfer.¹⁸ Among various redox-active functional groups, carbonyl-based compounds are the most well-known examples of bio-inspired redox centres.¹⁹ Due to their electron-withdrawing nature, carbonyl-containing structures have been demonstrated to enable the tailoring of materials with high redox potential, which is especially desirable for cathodes.¹² To optimize the properties, further introduction of N atoms into the building block could reduce the energy gap between the lowest unoccupied molecular orbital (LUMO) and the highest occupied molecular orbital (HOMO) of the molecule, leading to enhanced electronic and ionic conductivity.²⁰ Herein, we report a nitrogen- and carbonyl-rich extended π -conjugated small molecule, hexaazatrianthrylene (HATA) embedded quinone (HATAQ), as cathode for high-performance SIBs (Fig. 1a). The highly functionalized molecule with 12 redox-active sites ensures a high theoretical capacity for sodium storage. The additional unique intermolecular hydrogen bonds allow supramolecular layered arrangement of HATAQ molecules in two dimensions (2D), thus enhancing structural stability of this small organic molecule in SIB organic electrolyte during cell cycling.¹² The compound delivers a capacity as high as 460 mAh g⁻¹ at 500 mA g⁻¹ in a diglyme-based electrolyte. At an extremely high rate of 60 A g⁻¹, a reversible capacity of 138 mAh g⁻¹ corresponding to 99% retention is obtained after 5000 cycles, which is among the best ever reported for organic small molecules. Several characterization techniques in combination with density functional theory (DFT) studies shed light on the mechanism of HATAQ during discharge/charge, revealing the highly reversible multi-electron redox reaction. The effects of the solvent used in the electrolyte (ether-based vs. carbonate-based) on the electrochemical performance of HATAQ have also been elucidated.

Results and discussion

HATAQ was synthesized from low-cost and readily available starting materials using a facile procedure which could yield large-scale product of more than 50 g in a single batch.¹² The material characterization, namely, single-crystal and powder X-ray diffraction (PXRD), confirmed the graphite-like 2D layered packing with multiple unconventional hydrogen bonds (C-H...O interactions) between HATAQ molecules and π - π stackings.¹² These supramolecular arrangements in the solid state even though regarded as weak, could facilitate the structural stability and flexibility of the material during long-term battery cycling.

The electrochemical properties of HATAQ cathode were investigated by using coin cells with Na metal as anode and 0.9 M NaPF₆ in diethylene glycol dimethyl ether (DEGDME or diglyme) as electrolyte. Fig. 1b shows the voltage profiles of HATAQ at 500 mA g⁻¹ (1C, reaction with 12 Na in 1 h). The voltage plateaus observed are in good agreement with the major peak positions in the cyclic voltammogram (CV) in Fig. S1, approximately at 2.67/2.73, 2.08/2.19, 1.63/1.77 and 1.24/1.30 V vs. Na/Na⁺ for cathodic/anodic pairs. This CV feature suggests that the material undergoes multiple reversible redox processes during cell cycling.^{12,21} At the lowest rate of 500 mA g⁻¹, the compound delivers a discharge capacity of 460 mAh g⁻¹ in the voltage range of 0.9–3.7 V, which is close to the theoretical capacity of 516 mAh g⁻¹ for 12-electron transfer. At higher current densities of 1000 and 2000 mA g⁻¹, there is only a small decrease in initial capacities with 440 and 425 mAh g⁻¹, respectively. Fig. 1c and 1d show the capacity retention of HATAQ at various rates. The compound delivers reversible capacities of 420, 405 and 395 mAh g⁻¹ corresponding to a retention of 91.3, 92.1 and 92.9% after 200 cycles for 500, 1000 and 2000 mA g⁻¹, respectively. For long-term cycling, this redox-active molecule is found to be remarkably stable for up to 5000 cycles providing reversible capacities of 251, 224, 202 and 138 mAh g⁻¹, which correspond to retention values of 90.6, 92.6,

98.4 and 99.0 % for 10, 20, 40 and 60 A g⁻¹, respectively. Additional capacity retention performance is also provided for 60 A g⁻¹ up to 10000 cycles (Fig. S3). Fig. 1e shows the rate capability plot of HATAQ varying from 0.5 to 80 A g⁻¹. The result is found to be highly reversible with a capacity retention as high as 95.8 % when the cell resumes the rate of 0.5 A g⁻¹, which may be explained by the good charge transfer kinetics of Na ions and the extended π -conjugation of highly functionalized HATAQ.¹⁸ The gravimetric energy density is estimated, based on the specific capacity obtained at 500 mA g⁻¹ (1C) and the average discharge potential of \sim 2.0 V, to be \sim 920 Wh kg⁻¹ with respect to the cathode material, which is proved to be quite promising for large-scale energy storage applications.^{22,23} The excellent electrochemical performance as seen in HATAQ has rarely been observed in small-molecule-based organic batteries.

To understand the underlying mechanism of the Na-ion storage in HATAQ cathode, ex-situ Raman spectroscopy was carried out in the voltage range of 0.9–3.7 V. Fig. 2 shows the signals from the C=N and C=O groups of HATAQ at 1582 and 1660 cm⁻¹, respectively.^{12,24,25} As the cell undergoes discharge from open circuit voltage (OCV) to 0.9 V, the two signals become smaller indicating the interactions of the Na ions with the O and N atoms of HATAQ molecule during the reduction. As the cell undergoes charge process up to 3.7 V, the C=N and C=O bands become stronger, with intensities similar to those observed at OCV. This suggests the highly reversible storage of Na ions at the redox centres of the compound.

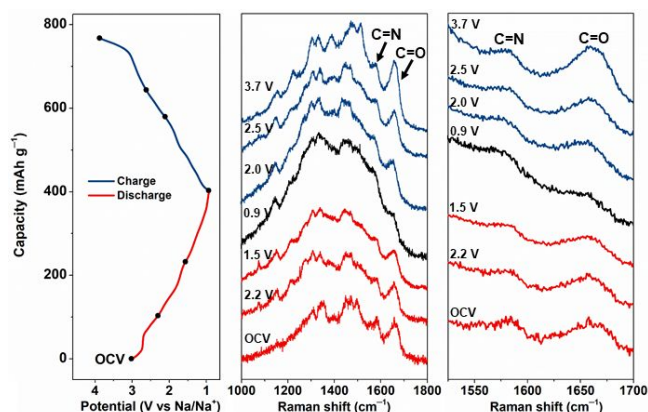


Fig. 2 Ex-situ Raman spectra of HATAQ electrodes at different voltage positions during discharge and charge and the corresponding voltage profile at 200 mA g⁻¹.

To gain further insight into the redox reactions during cycling, ex-situ X-ray photoelectron spectroscopy (XPS) was performed on the HATAQ electrodes that were cycled to different voltage positions during discharge/charge processes. Fig. S7 shows the high resolution C 1s spectrum of the pristine compound deconvoluted into five components approximately at 284.5, 285.1, 286.4, 287.9 and 290.5 eV, which correspond to C=C, C–C, C=N, C=O and C–F, respectively.^{20,24,26} As Na/HATAQ cell is discharged to 2.2 V, two new peaks appear at 285.2 eV (C–N) and 285.7 eV (C–O), while the C=N and C=O peaks become smaller.^{20,27} On further discharge to 1.5 and subsequently 0.9 V (lower cutoff voltage), the C–N and C–O signals appear stronger as the C=N and C=O are weaker, indicating the coordination of Na ions with the two redox-active carbonyl and imine

groups. When the cell is charged and the voltage rises to 2.0, 2.5 and 3.7 V, the C–N and C–O signals become weaker whereas the C=N and C=O components become larger. It is worth noting that due to the fact that the lone pair electrons of the N and O atoms in the imine and carbonyl groups can delocalize into the π -conjugated system, the binding energies of C=N and C=O in HATAQ are found to be close.¹² The high-resolution O 1s XPS spectra in Fig. S7 also reveal a similar behavior during cell cycling. The C=O peak (531.8 eV) of the pristine electrode becomes weaker during discharge, with the emergence of C–O (532.3 eV) as the cell voltage decreases to 0.9 V and HATAQ undergoes reduction in the presence of Na ions.^{26,28} During charge, the process is reversed with C=O becoming larger and C–O appearing weaker. The fact that the transformation of C–O to C=O and C–N to C=N during charge is found to be slightly incomplete may be explained by the kinetic limitations of electrochemical reaction in the solid state.¹²

Based on the ex-situ Raman and XPS results, both the carbonyl and imine groups can interact with Na ions because of the very small difference in the atomic charges and electronegativity of the O and N atoms in the extended π -conjugated HATAQ structure.¹² This is further confirmed by our density functional theory (DFT) calculations, which provide atomic-scale details on the HATAQ structural evolution during the sodiation process (Fig. S8 and S9). The first three sodiation steps lead to the formation of HATAQ–3Na, where each Na is located symmetrically in different clefts of the HATAQ molecule, forming dative Na–O and Na–N bonds with carbonyl and imine groups of the HATAQ molecule, respectively, consistent with the Raman and XPS results. The energies of these three redox processes are within \sim 0.3 V establishing the first redox plateau (Fig. S8). Subsequent addition of Na ions leads to a notable decrease of the redox potential, which is caused by the significant drop in the Na binding energy (as shown in Table S1) due to the simultaneous sharing of two Na ions by the individual HATAQ clefts in the HATAQ–6Na structure. The next two-step three-electron transfers corresponding to the formation of HATAQ–*n*Na (*n* = 7–9 and *n* = 10–12) were also established by our DFT calculations in agreement with the experimental discharge profile (Fig. 1) and the CV curve (Fig. S1). Interestingly, the HATAQ scaffold in the fully sodiated HATAQ–12Na complex maintains its planarity, while Na ions sit above and below the plane of the HATAQ molecule (Fig. S9). This suggests that Na intercalation should not significantly change the 2D supramolecular arrangement of HATAQ.

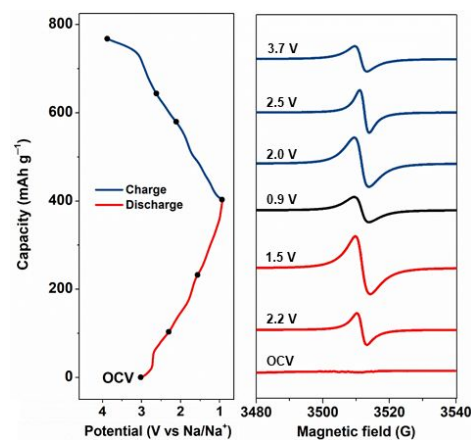


Fig. 3 Ex-situ EPR spectra of the HATAQ electrodes during cycling and the discharge/charge profile showing the voltage positions at 200 mA g⁻¹.

Organic electrode materials usually form radical intermediates which undergo transformation upon reduction/oxidation during discharge/charge processes.^{10,29} To further investigate the evolution of the electronic structure of HATAQ in the Na storage mechanism, ex-situ electron paramagnetic resonance (EPR) spectroscopy was carried out. Fig. 3 illustrates the change starting from OCV (~3.0 V) with the pristine HATAQ showing negative EPR signal, suggesting that there are no radical species present in HATAQ molecule. As the cell is discharged and HATAQ undergoes reduction process, the EPR signal becomes strongest at 1.5 V, indicating radical species being formed. The signal then decreases down to 0.9 V. As the cell is charged, the signal becomes stronger at 2.0 V and gradually dissipates on the way to 3.7 V. The change in EPR signal corresponds to the increase/decrease in the concentration of radical species in HATAQ, which indicates that the carbonyl and imine groups are transformed due to the acceptance/release of electrons at the redox centres and the interaction with Na ions.^{29,30} This confirms the redox activity of HATAQ molecule. These radical intermediates are known to have high reactivity and fast kinetics, which can support high-rate applications.²⁹

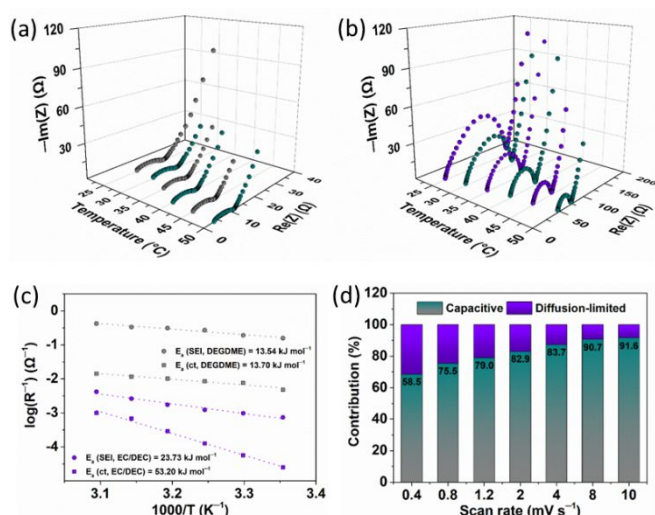


Fig. 4 Reaction kinetics study of HATAQ: (a) and (b) Temperature-dependent electrochemical impedance spectroscopy (EIS) of Na/HATAQ cells in 1 M NaPF₆ in DEGME and in EC/DEC electrolyte, respectively. (c) Arrhenius plots of the temperature dependence of EIS resistance showing the comparison between the charge transfer energy barrier ($E_{a,ct}$) and the activation energy across SEI layer ($E_{a,SEI}$) in the two electrolytes. (d) Capacity contributions from diffusion-controlled and capacitive processes calculated from the CV curves of HATAQ electrode at different scan rates in the DEGME electrolyte according to $i = k_1v + k_2v^{1/2}$.^{31,32}

The electrolyte environment (the sodium salt and solvent) is known to have a major impact on electrochemical performance, since there is still no universal electrolyte that is suitable for any electrode material for Na-based batteries.³³ In the process of performance optimization of HATAQ cathode, several electrolytes were tested (Fig. S10), such as carbonate-based, ether-based and carbonate-ether mixed-solvent systems. To obtain deeper understanding on these carbonate- and ether-based electrolytes, we performed a comparison study by investigating the electrochemical properties of HATAQ in two of the most common electrolytes for SIBs, namely, 1 M NaPF₆ in ethylene carbonate (EC)/diethyl carbonate (DEC) and 1 M NaPF₆ in DEGME.^{19,20,33,34} Fig. S11 shows the cycling performance of the material in both electrolytes at 500 mA g⁻¹. It is apparent that the capacity retention of HATAQ in

DEGDME-based electrolyte is far superior to that in EC/DEC, with a retention of 93% vs 68%, respectively, after 20 cycles as illustrated in Fig. S11c. Under the same sodium salt and concentration, 1 M NaPF₆, the main difference between these two electrolyte systems is the solvent. Solvation effect is known to influence the behavior of electrochemical systems by affecting the interfacial electrochemical characteristics and solvation shell structure.^{33,35,36} As evidenced by scanning electron microscopy (SEM) in Fig. S12, the HATAQ electrode in the EC/DEC-based electrolyte clearly has passivation layer covering the surface after 1 cycle which becomes much thicker after 20 cycles, while the electrodes from the DEGME-based electrolyte do not show an obvious morphology change over cycling.

This may be explained by the solvation shell in the bulk electrolyte and the desolvation process at the electrode/electrolyte interphase. To obtain the most stable configuration in the electrolyte, Na⁺ ion prefers to coordinate with six oxygen atoms.³³ Two molecules of DEGME (each one with three ether oxygens) are then required to form a stable solvation shell with Na⁺. In the case of the carbonate-based electrolyte, each carbonate solvent molecule (either EC or DEC) only provides one carbonyl oxygen to solvate Na⁺.³³ As a result, more carbonate molecules are needed to form a stable solvation shell with the same coordination number, which unavoidably leads to a stronger steric repulsion. Ultimately, due to the nature of the carbonyl oxygen which is a weak Lewis base and the steric hindrance, the solvation shell structure [Na⁺(EC/DEC)_x] does not possess a definite geometry.³³ Compared to EC/DEC, the multidentate chelating nature of the linear ether-based solvent DEGME with much less steric effects and the strong electron-donating ether oxygens will result in cation-solvent complex [Na⁺(DEGDME)_y] which is more rigid with much stronger binding between the cation and solvents.^{33,34} Therefore, DEGME system will show a higher solvation energy (implying that to desolvate one solvent molecule requires more energy) and higher reduction stability, while the carbonate electrolyte with lower solvation energy and lower reduction stability will undergo severe decomposition, thus forming a thicker solid electrolyte interphase (SEI).³⁴

To further confirm this observation, the reaction kinetics at the electrode/electrolyte interphase was revealed by temperature-dependent electrochemical impedance spectroscopy (EIS). Fig. 4a and 4b show the Nyquist plots as a function of temperatures of Na/HATAQ cell in 1 M NaPF₆ in DEGME in comparison with that in EC/DEC electrolyte. The Arrhenius plots in Fig. 4c indicate the charge transfer activation energy ($E_{a,ct}$) and the activation energy across SEI layer ($E_{a,SEI}$) in the two electrolyte systems. It has been found that a higher activation energy is required to transport Na⁺ ions across the SEI layer in the EC/DEC system (23.73 kJ mol⁻¹) compared to that in the DEGME system (13.54 kJ mol⁻¹). The sluggish/rapid transport of Na⁺ across the interphase will undoubtedly affect the rate performance during cell cycling. Moreover, the activation energy of charge transfer is found to be as high as 53.20 kJ mol⁻¹ for the carbonate-based electrolyte which is 3.88 times higher than that of the ether-based electrolyte (13.70 kJ mol⁻¹). The charge transfer process at the interphase of HATAQ electrode is also directly related to the microstructure and thickness of SEI.^{33,35,36} The thicker the SEI, the longer the distance for Na-ion diffusion. Overall, these findings suggest that due to a lower interphase resistance, the Na-ion transport across the interphase would be more rapid and efficient with better kinetic performance in DEGME electrolyte compared to EC/DEC system, leading to excellent rate capability.^{33,34}

As mentioned above, HATAQ could undergo rates as high as 60 A g⁻¹ with a relatively good reversible capacity of 138 mAh g⁻¹ and excellent capacity retention of 99% in the DEGME electrolyte. It is

noteworthy that at such a high cycling rate, the capacity contribution from the conducting additive is very small ($< 10 \text{ mAh g}^{-1}$, Fig. S4). The CV measurements at various scan rates (Fig. S13) were used to quantitatively differentiate the contribution of the capacitive and diffusion-controlled elements to the overall capacity provided by HATAQ (Fig. 4d). According to the relationship $i = k_1v + k_2v^{1/2}$, where i is the current at a fixed potential; v is the scan rate, with k_1v and $k_2v^{1/2}$ corresponding to the capacitive and diffusion-limited effects, respectively, the ratio of stored charge contributed by capacitive process is dominating at all the scan rates, which confirms the non-diffusion-controlled charge storage process of HATAQ.^{31,32,37} As the rate increases, a higher proportion of capacitive contribution is observed enabling an excellent rate performance.³⁷ Similar behavior where the capacity contribution is dominated by capacitive process can also be found in many organic-based electrodes.^{7,9,18,37} The electrons in HATAQ can delocalize in the highly extended π -conjugation through the π - π orbital interactions by resonance effect. This extended π -electron orbital overlap can help narrow the HOMO-LUMO gap, allowing good electronic mobility and redox reversibility, and facilitating the stabilization of the discharge product due to the resonance effect.¹² As a result, the possibilities of side reactions may be minimized and cycle life may be extended.³⁸

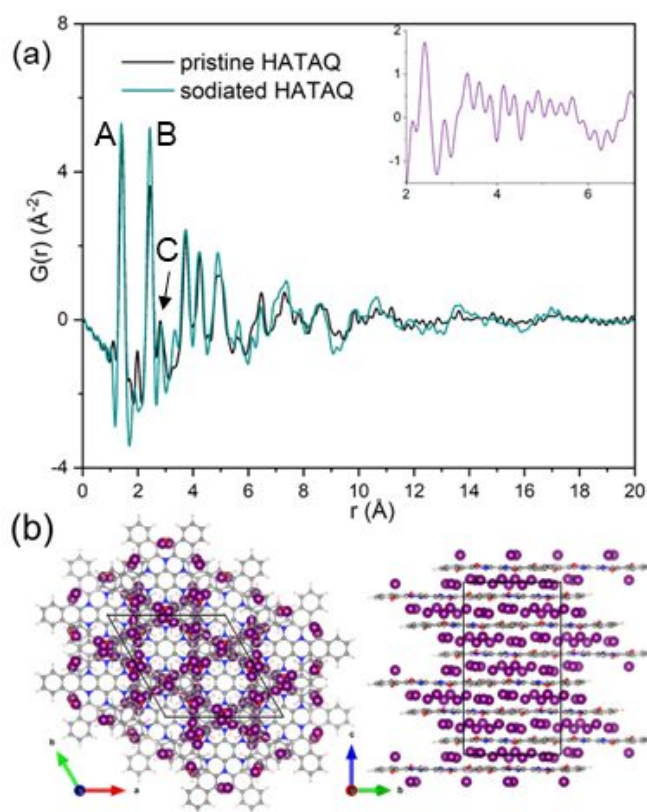


Fig. 5 Structural investigations of sodiated HATAQ: (a) X-ray PDFs of pristine (black) and sodiated (teal) HATAQ. The inset shows a simple difference PDF (purple) by subtracting sodiated HATAQ PDF data from a PDF of pristine HATAQ, showing weak signals related to Na-to-HATAQ pair correlations at short distances. (b) Top and side views of the fully sodiated HATAQ structure obtained from periodic DFT calculations. Colour scheme: C, grey; H, white; N, blue; O, red; Na, purple.

The structural stability of the compound was investigated by ex-situ PXRD experiments as shown in Fig. S14. The PXRD pattern of the pristine electrode agrees well with that of HATAQ powder obtained

by heating at $120 \text{ }^\circ\text{C}$ in vacuum. With a cycling rate of 200 mA g^{-1} at the end of discharge (0.9 V), an obvious change is observed with the peak at $\sim 27^\circ$ corresponding to diffraction from the (006) plane of HATAQ slightly shifted toward a lower 2θ .¹² This peak subsequently shifts back to a higher angle at the end of charge (3.7 V). This may be explained by an increase in the interlayer spacing of HATAQ structure due to the interactions with Na ions during discharge and a decrease of the interlayer distance due to Na-ion extraction during charge. The fact that this (006) peak is visible during cycling indicates that HATAQ is still crystalline and π -stacking still remains.

To investigate both real-space long- and short-range structural features of the HATAQ material before and after sodium intercalation (fully discharged state), we performed ex-situ synchrotron total X-ray scattering measurements at the National Synchrotron Light Source II (NSLS-II), USA. The high-energy X-rays at NSLS-II enabled us to collect high momentum transfer (Q)-range data (Fig. S15) required to produce real-space pair distribution functions (PDFs) presented in Fig. 5a. As expected, HATAQ exhibits real-space local structural features consistent with common graphitic carbon materials.^{39,40} In particular, the first three intense peaks (A, B, C) in the HATAQ PDF correspond to the in-plane distances of the aromatic rings at 1.42 , 2.44 and $2.82 \text{ } \text{\AA}$, respectively. Next small feature at $\sim 3.4 \text{ } \text{\AA}$ for the pristine HATAQ is related to the interlayer correlations or a distance between the HATAQ layers. Upon incorporation of sodium ions, this peak becomes more apparent and shifts to a longer distance in agreement with our in-lab PXRD results discussed above. At long- r region, variations in PDF peak intensities between pristine and sodiated HATAQs are also noticeable due to an increase of spacing between adjacent two HATAQ layers after Na uptake and added contribution from Na-to-HATAQ atom-atom correlations. At short- r region, there is little difference between the PDFs in general, except for the intensity of peak B, which could be explained by emerging Na-HATAQ interactions, namely the appearance of Na-C, Na-O and Na-N correlations at a local scale, based on their relative X-ray weighting factors (Fig. S16). Indeed, the differential PDF (d-PDF) analysis in Fig. 5a (inset) shows that added contribution from sodium-to-HATAQ correlations appears at $\sim 2.4 \text{ } \text{\AA}$ which overlaps with the position of peak B in the total PDF. Moreover, Na-C, Na-O and Na-N distance distributions represented by the first peak in the d-PDF can be well matched with the corresponding distances (Fig. S17) in the sodiated HATAQ structure shown in Fig. 5b that was obtained by the periodic DFT calculations, further confirming that Na ions can readily intercalate between the HATAQ layers. Interestingly, Na ions are bound by both carbonyl and imine groups of HATAQ according to the DFT optimized structure, forming peculiar interconnected sodium hexagrams that can be seen from a top view of the sodiated HATAQ structure. Additional ab-initio molecular dynamics (MD) simulations of the Na-HATAQ structure at elevated temperatures show the robustness of the 2D stacking arrangement in HATAQ (Fig. S18), supporting the enhanced cycling stability of the HATAQ cathode observed in our electrochemical experiments due to the unique hydrogen-bonding enabled graphite-like structure of the material.

Conclusions

We report a nitrogen- and carbonyl-rich highly extended π -conjugated small molecule, hexaazatrianthrylene (HATA) embedded quinone (HATAQ), as cathode material for SIBs. The unique supramolecular graphite-like structure of the material has been shown to be robust as observed in the excellent

cycling stability of HATAQ cathode. Both the carbonyl and imine groups are found to readily interact with Na ions during the redox processes via radical intermediates offering high reactivity and fast kinetics. The π -electron orbital overlap in the highly extended conjugation of HATAQ can allow electrons to delocalize through the π - π orbital interactions, leading to facile charge transport and redox reversibility, as well as stabilizing the discharge product by resonance effect. The redox kinetics at the interphase of HATAQ electrode is found to be superior in the diglyme-based electrolyte as evidenced by the low interphase resistance (small activation energies for charge transfer and ionic transport), thus leading to excellent rate capability. The valuable mechanistic and structural insights gained from this study may unleash more possibilities of high-performance organic-small-molecule cathodes for next-generation sustainable energy storage technologies.

Experimental

General methods and materials

The chemicals and solvents were purchased and used without further purification from commercial suppliers (Sigma-Aldrich and Alfa Aesar). The HATAQ cathode material was synthesized according to our original procedure reported previously, by a reaction between 2,3-diamino-1,4-naphthoquinone and cyclohexane hexaketone.¹² PXRD data collection was performed on Bruker D8 Advance ECO. The Raman spectra were collected by UniDRON Raman microscope with an excitation laser beam wavelength of 633 nm. XPS measurements were carried out on ULVAC PHI 5000 VersaProbe III with Al K α (1487 eV) as an X-ray source. Survey scans were collected with a pass energy of 100 eV, followed by high-resolution scans of the C 1s and O 1s regions with a pass energy of 20 eV. All spectra were charge-corrected relative to the C 1s component at 284.5 eV binding energy and analyzed using CasaXPS software. The EPR spectra were recorded on a Bruker EMX System EPR with X-band EPR spectrometer operating at 9.80 GHz. Microwave power was set to 2.002 mW. Sweep width was performed with 100G and a center field of 3510G. The field modulation frequency was set to 100 kHz, and the modulation amplitude was 6G. SEM was performed on a SU8010 HR-FESEM scanning electron microscope.

Synchrotron X-ray scattering measurements

High-energy X-ray total scattering data were collected at the 28-ID-1 beamline of the National Synchrotron Light Source II (NSLS-II), Brookhaven National Laboratory, USA. A horizontally focusing side bounce monochromator was used to deliver X-rays with the energy of 74.4 keV (0.1667 Å) and a beam of cross-sectional area 0.25×0.25 mm². An amorphous 2D silicon-based area detector (PerkinElmerXRD 1621, 200×200 micron pixels) was positioned about 20.8 cm from the sample to collect total scattering intensity data, which yielded an accessible momentum transfer (Q) range up to 25 Å⁻¹. Powder samples of the pristine HATAQ and fully discharged HATAQ electrode (washed with DEGDME and dried in a glovebox for 24 h) were enclosed in polyimide capillaries and measured in transmission

mode at room temperature. The dark current scans were collected and subtracted from the raw X-ray patterns, which allows residual intensity to be removed and prevents pixel overexcitation.⁴¹ Data for an empty polyimide container were also collected for the background correction. Calibration of the sample to detector distance and detector alignment with data from a CeO₂ powder (NIST SRM 674) standard was done in *pyFAI* software.⁴² Raw scattering data were radially integrated into Q-space spectra, applying a mask and polarization correction during integration using *xpdtools* package.⁴³ The normalized total scattering patterns – structure functions, S(Q)'s, were obtained in *PDFgetX2*⁴⁴ by subtracting polyimide container scattering, employing the appropriate sample composition and corrections (sample self-absorption, multiple scattering and inelastic Compton scattering) following standard procedures.^{45,46} The resultant real space pair distribution functions, G(r)s, in Fig. 5 were calculated via Fourier transformation (Eq. 1) of the S(Q) utilizing a Q_{max} of 25 Å⁻¹.

$$G(r) = \frac{2}{\pi} \int_{Q_{\min}}^{Q_{\max}} Q[S(Q) - 1] \sin(Qr) dQ \quad (1)$$

Density functional theory (DFT) calculations

Molecular calculations. Electronic structure calculations of the HATAQ and HATAQ-*n*Na (*n* = 1–12) molecular complexes were performed with the Gaussian 16 rev A.03.⁴⁷ We used the DFT approach for our calculations at the B3LYP/6-31+G(d,p) level of theory. Frequency calculations were performed at the B3LYP/6-31+G(d) level to ensure that geometries (optimized at the same level of theory) were minima and to compute zero-point energies and thermal corrections (T = 298.15 K) to Gibbs free energy. Dimethoxyethane (DME) solvent was chosen in the polarizable continuum model⁴⁸ using the integral equation formalism variant (IEFPCM) with the solvent parameters taken from C. Peng et al.⁴⁹ The static dielectric constant (ϵ) was set to 7.20, the molecular radius of the solvent: 2.78255 Å, the density of the solvent: 0.005804 particles/Å and the molar volume of the solvent: 103.7911 cm⁻³. The redox calculations require the global minimum geometries for each sodiated HATAQ species. Therefore, we performed an unbiased quantum-chemical search for the most energetically stable HATAQ complexes with Na using the Coalescence Kick (CK) program,^{50,51} which employs a stochastic approach for finding the global minimum. Some additional structures not found by the CK algorithm were constructed and optimized, and their relative energies were compared to confirm the lowest energy structure among other possible configurations. The reduction potential of redox-active HATAQ molecule in the solution was calculated using the formula:

$$E^{\text{redox}} = - (G^{\text{final}} - G^{\text{initial}} - G^{\text{Na}}) / nF \quad (2)$$

where G^{final} , G^{initial} and G^{Na} are the calculated Gibbs free energies (kcal mol⁻¹) of the final and initial sodiated states of the HATAQ molecule, and Na atom, respectively; *n* is the number of electrons transferred in the process; *F* is the Faraday constant.

Periodic DFT calculations. Periodic DFT calculations were performed using the Vienna Ab-initio Simulation Package (VASP).⁵²⁻⁵⁵ The valence electronic states were expanded in a basis of plane waves, while the core valence interactions were described using the Projector Augmented Wave (PAW) approach.^{56,57} The plane wave kinetic energy cut off was set to 600 eV and the PBE GGA functional⁵⁸ was employed to describe the exchange correlation interactions. The DFT-D3 approach of Grimme with zero damping⁵⁹ was used to account for the van der Waals interactions. The SCF convergence threshold was set to 10^{-5} eV and a Pulay scheme⁶⁰ was used for charge density mixing during the SCF solution. The chosen level of theory was shown to provide sufficient accuracy in predicting structural parameters for the HATAQ structure as compared to the experimental X-ray single-crystal diffraction results.¹² MD simulations in VASP utilized a plane wave energy cutoff of 500 eV, and the Brillouin zone was sampled using the Gamma point approximation. An MD time step of 1 fs was used, and the temperature (450 K) was controlled using the Nose-Hoover thermostat. The MD simulations lasted for a duration of 6 ps (6000 time steps in total).

Electrochemical studies

HATAQ, Ketjen black conductive carbon and poly(vinylidenedifluoride) (PVDF) in the ratio of 3:6:1 were mixed and ground in the presence of *N*-methyl-2-pyrrolidinone (NMP). Other ratios of electrode mixture, 4.5:4.5:1, 6:3:1 and 7:2:1, were also tested. The mass loading of the active material was kept at ~ 1.5 – 2.0 mg cm⁻² for 3:6:1, while the active mass loading for the 7:2:1 ratio is ~ 3.0 mg cm⁻². The slurry was coated onto carbon paper (MGL280) current collector and dried at 100 °C in vacuum overnight. Na metal was used as anode to assemble coin cells with 0.9 M NaPF₆ in DEGDME as electrolyte and Whatman glass microfiber (GF/D) membrane as separator inside an argon-filled glovebox with O₂ and H₂O levels below 0.1 ppm. Different electrolytes with a different Na salt and concentrations in various organic solvents were also used to investigate the electrochemical performance of HATAQ. The galvanostatic discharge/charge cycling, CV and EIS measurements were performed on an Arbin battery cycler and a Biologic VMP3 potentiostat. EIS was performed over a frequency range of 1 kHz–10 mHz. The coin cells were allowed to rest for at least 3 h before measurements. For activation energy calculations, EIS data were collected at 25, 30, 35, 40, 45 and 50 °C inside a temperature chamber. At each temperature, the cells were allowed to equilibrate for at least 1 h.

Electrode mechanistic studies

For all ex-situ analyses, the Na/HATAQ cells were discharged/charged to various voltage positions using a rate of 200 mA g⁻¹ unless otherwise stated. For ex-situ Raman, the HATAQ electrodes consisted of 70 wt% active material, 20 wt% copper and 10 wt% PVDF.¹⁰ For ex-situ XPS, EPR and synchrotron X-ray scattering measurements, the electrodes contained 70 wt% active material, 20 wt% Ketjen black and 10 wt% PVDF (active mass loading of ~ 4.0 mg cm⁻²). For all these ex-situ experiments mentioned above, stainless steel was used as current collector. For ex-situ SEM, the electrodes were

prepared by using 30 wt% active material, 60 wt% Ketjen black and 10 wt% PVDF with MGL280 as current collector. The coated electrodes were dried in vacuum at 80 °C overnight. For ex-situ PXRD, self-standing electrodes with the thickness of 0.2 mm were used. The electrode mixture was made by combining 70 wt% active material, 20 wt% Ketjen black and 10 wt% poly(tetrafluoroethylene) (PTFE) in the presence of ethanol (active mass loading of ~ 9.0 mg cm⁻²). The electrodes after being cut into discs were dried in vacuum overnight at 80 °C. CR2032 coin cells were assembled by using Na metal as anode, 0.9 M NaPF₆ in DEGDME as electrolyte and Whatman glass microfiber (GF/A) membrane as separator. For all the ex-situ measurements, the cells were disassembled, washed by DME, and dried overnight in argon-filled glovebox. All the samples were handled without any exposure to air.

Author contributions

H.-C. K. performed all the electrochemical and mechanistic studies with the assistance from N. T. H. L. W. K., T.-H. C. and I. P. provided intellectual input. The computational simulations and synchrotron X-ray scattering measurements using PDF technique were performed and analyzed by A. S. I. I. P. synthesized the compound HATAQ. J.-C. L. conducted the XPS experiments. W. K. interpreted the experiments and wrote the manuscript, incorporating the input from all the other authors.

Conflicts of interest

The authors declare no conflict of interest.

Acknowledgements

This work was supported by the Ministry of Science and Technology (MOST) of Taiwan under grant MOST 109-2113-M-006-016 (to T.-H. C.) and the Young Scholar Fellowship Program MOST 109-2636-E-006-001 (to W. K.). This work was also financially supported by the Hierarchical Green-Energy Materials (Hi-GEM) Research Center, from the Featured Areas Research Center Program within the framework of the Higher Education Sprout Project by the Ministry of Education (MOE) and MOST (MOST 111-2634-F-006-008) in Taiwan (to W. K.). This research was supported in part by High Education Sprout Project, Ministry of Education of the Headquarters of University Advancement at National Cheng Kung University (NCKU) (to T.-H. C. and W. K.). The research of A.S.I. was supported as part of the Fluid Interface Reactions, Structures and Transport, an Energy Frontier Research Center funded by the U.S. Department of Energy (DOE), Office of Science, Office of Basic Energy Sciences at Oak Ridge National Laboratory under contract # DE-AC05-00OR22725. I.P. was supported by the U.S. DOE, Office of Science, Office of Basic Energy Sciences, Materials Sciences and Engineering Division under contract # DE-AC05-00OR22725. The 28-ID-1 beamline of the National Synchrotron Light Source II was used, which is a U.S. DOE Office of Science User Facility operated for the DOE Office of Science by Brookhaven National Laboratory under Contract # DE-SC0012704. This research used

resources of the Computer and Data Environment for Science (CADES) at Oak Ridge National Laboratory. The authors acknowledge the use of ESCA000200 and SQUID001200 of MOST 110-2731-M-006-001 belonging to the Core Facility Center of NCKU. This manuscript has been authored in part by UT-Battelle, LLC, under contract DE-AC05-00OR22725 with the US DOE. The US government retains and the publisher, by accepting the article for publication, acknowledges that the US government retains a nonexclusive, paid-up, irrevocable, worldwide license to publish or reproduce the published form of this manuscript, or allow others to do so, for US government purposes. DOE will provide public access to these results of federally sponsored research in accordance with the DOE Public Access Plan (<http://energy.gov/downloads/doe-public-access-plan>).

Notes and references

1. H. Wang, P. Hu, J. Yang, G. Gong, L. Guo and X. Chen, *Adv. Mater.*, 2015, **27**, 2348–2354.
2. Y. Liang and Y. Yao, *Joule*, 2018, **2**, 1690–1706.
3. C.-H. Chang, A.-C. Li, I. Popovs, W. Kaveevivitchai, J.-L. Chen, K.-C. Chou, T.-S. Kuo and T.-H. Chen, *J. Mater. Chem. A*, 2019, **7**, 23770–23774.
4. A.-C. Li, C.-H. Chang, A. S. Ivanov, Y.-A. Lo, I. Popovs, J.-L. Chen, Y.-C. Chuang, Y.-C. Chang, B.-H. Chen, J.-C. Lee, T.-H. Chen and W. Kaveevivitchai, *J. Mater. Chem. A*, 2022, DOI: 10.1039/D2TA01463G.
5. M. Lee, J. Hong, J. Lopez, Y. Sun, D. Feng, K. Lim, W. C. Chueh, M. F. Toney, Y. Cui and Z. Bao, *Nat. Energy*, 2017, **2**, 861–868.
6. T. Sun, Z.-j. Li, H.-g. Wang, D. Bao, F.-l. Meng and X.-b. Zhang, *Angew. Chem. Int. Ed.*, 2016, **55**, 10662–10666.
7. Y. Hu, Q. Yu, W. Tang, M. Cheng, X. Wang, S. Liu, J. Gao, M. Wang, M. Xiong, J. Hu, C. Liu, T. Zou and C. Fan, *Energy Storage Mater.*, 2021, **41**, 738–747.
8. C. Ma, L.-Y. Wang, M.-H. Shu, C.-C. Hou, K.-X. Wang and J.-S. Chen, *J. Mater. Chem. A*, 2021, **9**, 11530–11536.
9. Y. Chen, H. Li, M. Tang, S. Zhuo, Y. Wu, E. Wang, S. Wang, C. Wang and W. Hu, *J. Mater. Chem. A*, 2019, **7**, 20891–20898.
10. S. Wu, W. Wang, M. Li, L. Cao, F. Lyu, M. Yang, Z. Wang, Y. Shi, B. Nan, S. Yu, Z. Sun, Y. Liu and Z. Lu, *Nat. Commun.*, 2016, **7**, 13318.
11. R. R. Kapaev, I. S. Zhidkov, E. Z. Kurmaev, K. J. Stevenson and P. A. Troshin, *J. Mater. Chem. A*, 2019, **7**, 22596–22603.
12. M.-S. Wu, N. T. H. Luu, T.-H. Chen, H. Lyu, T.-W. Huang, S. Dai, X.-G. Sun, A. S. Ivanov, J.-C. Lee, I. Popovs and W. Kaveevivitchai, *Adv. Energy Mater.*, 2021, **11**, 2100330.
13. N. T. H. Luu, A. S. Ivanov, T.-H. Chen, I. Popovs, J.-C. Lee and W. Kaveevivitchai, *J. Mater. Chem. A*, 2022, DOI: 10.1039/D2TA01621D.
14. K. S. Weeraratne, A. A. Alzharani and H. M. El-Kaderi, *ACS Appl. Mater. Interfaces*, 2019, **11**, 23520–23526.
15. S. Lee, G. Kwon, K. Ku, K. Yoon, S.-K. Jung, H.-D. Lim and K. Kang, *Adv. Mater.*, 2018, **30**, 1704682.
16. F.-Y. Chou, J.-C. Tang, H.-Y. Lee, J.-C. Lee, S. Ratchahat, T.-H. Chen and W. Kaveevivitchai, *ACS Appl. Energy Mater.*, 2020, **3**, 11300–11306.
17. F. Xu, H. Wang, J. Lin, X. Luo, S.-a. Cao and H. Yang, *J. Mater. Chem. A*, 2016, **4**, 11491–11497.
18. M. K. Shehab, K. S. Weeraratne, T. Huang, K. U. Lao and H. M. El-Kaderi, *ACS Appl. Mater. Interfaces*, 2021, **13**, 15083–15091.
19. J. Hong, M. Lee, B. Lee, D.-H. Seo, C. B. Park and K. Kang, *Nat. Commun.*, 2014, **5**, 5335.
20. R. Shi, L. Liu, Y. Lu, C. Wang, Y. Li, L. Li, Z. Yan and J. Chen, *Nat. Commun.*, 2020, **11**, 178.
21. Q. Zhao, W. Zhao, C. Zhang, Y. Wu, Q. Yuan, A. K. Whittaker and X. S. Zhao, *Energy Fuels*, 2020, **34**, 5099–5105.
22. Y. Lu and J. Chen, *Nat. Rev. Chem.*, 2020, **4**, 127–142.
23. P. Poizot, J. Gaubicher, S. Renault, L. Dubois, Y. Liang and Y. Yao, *Chem. Rev.*, 2020, **120**, 6490–6557.
24. Z. Lei, Q. Yang, Y. Xu, S. Guo, W. Sun, H. Liu, L.-P. Lv, Y. Zhang and Y. Wang, *Nat. Commun.*, 2018, **9**, 576.
25. B. Zhuang, M. Fujitsuka, S. Tojo, D. W. Cho, J. Choi and T. Majima, *J. Phys. Chem. A*, 2018, **122**, 8738–8744.
26. Q. Xue, D. Li, Y. Huang, X. Zhang, Y. Ye, E. Fan, L. Li, F. Wu and R. Chen, *J. Mater. Chem. A*, 2018, **6**, 12559–12564.
27. R. Guo, Y. Wang, S. Heng, G. Zhu, V. S. Battaglia and H. Zheng, *J. Power Sources*, 2019, **436**, 226848.
28. K. W. Nam, H. Kim, Y. Beldjoudi, T.-w. Kwon, D. J. Kim and J. F. Stoddart, *J. Am. Chem. Soc.*, 2020, **142**, 2541–2548.
29. S. Gu, S. Wu, L. Cao, M. Li, N. Qin, J. Zhu, Z. Wang, Y. Li, Z. Li, J. Chen and Z. Lu, *J. Am. Chem. Soc.*, 2019, **141**, 9623–9628.
30. Q. Jiang, P. Xiong, J. Liu, Z. Xie, Q. Wang, X.-Q. Yang, E. Hu, Y. Cao, J. Sun, Y. Xu and L. Chen, *Angew. Chem. Int. Ed.*, 2020, **59**, 5273–5277.
31. J. Wang, J. Polleux, J. Lim and B. Dunn, *J. Phys. Chem. C*, 2007, **111**, 14925–14931.
32. E. Lim, C. Jo, H. Kim, M.-H. Kim, Y. Mun, J. Chun, Y. Ye, J. Hwang, K.-S. Ha, K. C. Roh, K. Kang, S. Yoon and J. Lee, *ACS Nano*, 2015, **9**, 7497–7505.
33. T. Sun, X.-L. Feng, Q.-Q. Sun, Y. Yu, G.-B. Yuan, Q. Xiong, D.-P. Liu, X.-B. Zhang and Y. Zhang, *Angew. Chem. Int. Ed.*, 2021, **60**, 26806–26812.
34. J. Yang, J. Ruan, Q. Li, F. Fang, Y. Song, D. Sun and F. Wang, *Adv. Funct. Mater.*, 2022, DOI: <https://doi.org/10.1002/adfm.202200566>, 2200566.
35. K. Xu, Y. Lam, S. S. Zhang, T. R. Jow and T. B. Curtis, *J. Phys. Chem. C*, 2007, **111**, 7411–7421.
36. K. Xu, *J. Electrochem. Soc.*, 2007, **154**, A162.
37. W. Wang, V. S. Kale, Z. Cao, S. Kandambeth, W. Zhang, J. Ming, P. T. Parvatkar, E. Abou-Hamad, O. Shekhah, L. Cavallo, M. Eddaoudi and H. N. Alshareef, *ACS Energy Lett.*, 2020, **5**, 2256–2264.
38. H. Lyu, X.-G. Sun and S. Dai, *Adv. Energy Sustain. Res.*, 2021, **2**, 2000044.
39. V. Petkov, R. G. Difrancesco, S. J. L. Billinge, M. Acharya and H. C. Foley, *Philos. Mag. B*, 1999, **79**, 1519–1530.
40. R. Wyckoff, *Crystal Structures*, Wiley, New York, 1954.
41. L. B. Skinner, C. J. Benmore and J. B. Parise, *Nucl. Instrum. Methods Phys. Res. A*, 2012, **662**, 61–70.
42. G. Ashiotis, A. Deschildre, Z. Nawaz, J. P. Wright, D. Karkoulis, F. E. Picca and J. Kieffer, *J. Appl. Cryst.*, 2015, **48**, 510–519.
43. C. J. Wright and X.-D. Zhou, *J. Synchrotron Rad.*, 2017, **24**, 506–508.
44. X. Qiu, J. W. Thompson and S. J. L. Billinge, *J. Appl. Cryst.*, 2004, **37**, 678.
45. T. Egami and S. J. Billinge, *Underneath the Bragg Peaks: Structural Analysis of Complex Materials*, Newnes, 2012.
46. H. E. Fischer, A. C. Barnes and P. S. Salmon, *Rep. Prog. Phys.*, 2005, **69**, 233–299.
47. M. J. Frisch, G. W. Trucks, H. B. Schlegel, G. E. Scuseria, M. A. Robb, J. R. Cheeseman, G. Scalmani, V. Barone, G. A. Petersson,

- H. Nakatsuji, X. Li, M. Caricato, A. V. Marenich, J. Bloino, B. G. Janesko, R. Gomperts, B. Mennucci, H. P. Hratchian, J. V. Ortiz, A. F. Izmaylov, J. L. Sonnenberg, Williams, F. Ding, F. Lipparini, F. Egidi, J. Goings, B. Peng, A. Petrone, T. Henderson, D. Ranasinghe, V. G. Zakrzewski, J. Gao, N. Rega, G. Zheng, W. Liang, M. Hada, M. Ehara, K. Toyota, R. Fukuda, J. Hasegawa, M. Ishida, T. Nakajima, Y. Honda, O. Kitao, H. Nakai, T. Vreven, K. Throssell, J. A. Montgomery Jr., J. E. Peralta, F. Ogliaro, M. J. Bearpark, J. J. Heyd, E. N. Brothers, K. N. Kudin, V. N. Staroverov, T. A. Keith, R. Kobayashi, J. Normand, K. Raghavachari, A. P. Rendell, J. C. Burant, S. S. Iyengar, J. Tomasi, M. Cossi, J. M. Millam, M. Klene, C. Adamo, R. Cammi, J. W. Ochterski, R. L. Martin, K. Morokuma, O. Farkas, J. B. Foresman and D. J. Fox, *Gaussian 16 Rev. A.03*, Wallingford, CT, 2016.
48. A. V. Marenich, C. J. Cramer and D. G. Truhlar, *J. Phys. Chem. B*, 2009, **113**, 6378–6396.
49. C. Peng, G.-H. Ning, J. Su, G. Zhong, W. Tang, B. Tian, C. Su, D. Yu, L. Zu, J. Yang, M.-F. Ng, Y.-S. Hu, Y. Yang, M. Armand and K. P. Loh, *Nat. Energy*, 2017, **2**, 17074.
50. A. P. Sergeeva, B. B. Averkiev, H.-J. Zhai, A. I. Boldyrev and L.-S. Wang, *J. Chem. Phys.*, 2011, **134**, 224304.
51. A. S. Ivanov, A. J. Morris, K. V. Bozhenko, C. J. Pickard and A. I. Boldyrev, *Angew. Chem. Int. Ed.*, 2012, **51**, 8330–8333.
52. G. Kresse and J. Hafner, *Phys. Rev. B*, 1993, **47**, 558–561.
53. G. Kresse and J. Hafner, *Phys. Rev. B*, 1994, **49**, 14251–14269.
54. G. Kresse and J. Furthmüller, *Phys. Rev. B*, 1996, **54**, 11169–11186.
55. G. Kresse and J. Furthmüller, *Comput. Mater. Sci.*, 1996, **6**, 15–50.
56. P. E. Blöchl, *Phys. Rev. B*, 1994, **50**, 17953–17979.
57. G. Kresse and D. Joubert, *Phys. Rev. B*, 1999, **59**, 1758–1775.
58. J. P. Perdew, K. Burke and M. Ernzerhof, *Phys. Rev. Lett.*, 1996, **77**, 3865–3868.
59. S. Grimme, J. Antony, S. Ehrlich and H. Krieg, *J. Chem. Phys.*, 2010, **132**, 154104.
60. P. Pulay, *Chem. Phys. Lett.*, 1980, **73**, 393–398.